

Performances Analysis of Non-Model-Based Speed Estimation Algorithms for Motor Drives

Gaetano Turrisi¹, Luigi Danilo Tornello¹, Giacomo Scelba¹,
Giulio De Donato², Giuseppe Scarcella¹

University of Catania, Viale Andrea Doria 6, Catania, Italy ¹

University of Rome “La Sapienza”, Via Eudossiana 18, Roma, Italy ²

E-Mail: giacomo.scelba@unict.it, giulio.dedonato@uniroma1.it

Keywords

«Variable speed drives», «resolution», «position measurement», «speed estimation», «motion control», «speed control», «digital filters», «stability analysis».

Abstract

This paper investigates the performances of speed-controlled motor drives using non-model-based speed estimation algorithms. A suitable modelling of the speed estimation algorithms combined to the analytical representation of the instantaneous quantized speed of finite resolution position sensors are exploited to evaluate the filtering action of the estimation algorithms, and the stability and rejection to torque disturbances of speed-controlled drives at low rotational speeds; the last operating condition is very critical for motor drives, especially for that using low resolution position sensors. In this study, the theoretical analysis is experimentally validated on a 2kW PMSM drive.

Introduction

In several applications a closed loop speed control is required, as well as the rotor position for field orientation in AC motor drives [1]-[3] and for switching in different categories of synchronous drives, such as BLDC, SRM and wound field doubly salient generator drives [4]-[8]. This is accomplished using a single position sensor, and by estimating the speed through an appropriate speed estimation algorithm [1]. Alternatively, the position and speed can be carried out through model-based and high frequency injection-based sensorless algorithms [7]-[14].

Regardless of the technology employed in the position sensor (incremental/absolute encoders, resolvers, inductive position sensors or Hall effect sensors), the selection of it is influenced by several factors, such as accuracy, resolution, operating temperatures, sensibility to mechanical, magnetic and electrical disturbances, maximum speed rating, and cost [15]. In particular, the choice of the position sensor resolution can significantly impact on the accuracy and bandwidth of the estimated speed and cost of the drive, especially in low-cost applications where a considerable reduction of cost and size of the sensor is desirable [4], [5], [16], [17].

The rotor position measurement is characterized by a finite resolution that can be expressed in number of discrete states per revolution, N_{ds} . Besides the sensor, the speed estimation method plays a key role as it contributes to satisfy the desired performance requirements. Various speed estimation methods are available in the technical literature, which can be classified in two main categories: model-based and non-model-based speed estimation algorithms; the last category is still widely used in many industrial applications not only for their simple implementation but also because they do not need additional information on the properties of the mechanical load [18]-[19]. Some of non-model-based speed estimation algorithms are implemented according to the first-order Taylor approximation of rotor speed:

$$\omega_{re}(t) = \frac{d\theta_{re}(t)}{dt} \approx \hat{\omega}_{re} = \frac{\theta_{re}(t_1) - \theta_{re}(t_2)}{t_1 - t_2} = \frac{\Delta\theta_{re}}{\Delta t} \quad (1)$$

where θ_{re} is the rotor angle, while ω_{re} and $\hat{\omega}_{re}$ are the actual and estimated rotor speeds. Two straightforward speed estimation implementations can be carried out starting from (1): the first, named

as fixed time method (FTM) [18]-[27], is based on counting the number of position measurement updates in a set time interval, while the second method measures the time elapsed between two consecutive position measurement updates, and is known as fixed position method (FPM), or period-based speed estimation, [18]-[27]. While FTM is very accurate at high speeds, FPM is effective at low and medium speeds; motor drives can combine both methods to cover the full speed range, [18]. More advanced speed estimation algorithms have been also presented in the literatures, mainly based on higher-order Taylor approximations (TSE) [20], [23], polynomial interpolation [23]-[24], and least-squares fit (LSF) [20]-[24], where the main aim of all of these methods is to properly interpolate the quantized discontinuous position measurement. Most studies are mainly focused to the analysis of the filter characteristics of those algorithms, without providing an in-depth analysis of the dynamic response, stability and disturbance rejection capability associated to these estimation methods, which are also related to the concept of instantaneous quantized speed of finite resolution position sensors. With this paper, the authors strive to fill this gap, presenting a methodology for investigating the performances of FPM speed estimation algorithms, starting from their small signal modelling around an operating point. Although of general validity, the proposed approach has been applied to three different FPM algorithms, based on Taylor series expansion (TSE1) [28]-[29], and least-squares fit (LSF1/4 and LSF1/8) [20]-[22].

The rest of the paper is organized as follows: In the next section, a brief description of three different FPM algorithms considered in this study is presented; then, small signal models for each implementation are carried out. The performances of these estimation algorithms are thus analysed in the speed-controlled drive, according to their filtering, stability, and disturbance rejection capability. The theoretical study is experimentally evaluated on a 2.6kW PMSM drive, and conclusions are finally given in the last section.

Fixed Position-Based Speed Estimation Algorithms

The FPM implementation provides the estimated speed by measuring the time τ_d between two consecutive updates of the quantized angular position $\theta_{re}^{(q)}(t)$. The time τ_d is determined as in (2), by counting the number of clocks n of a high-frequency counter with frequency $f_{CLK}=1/T_{CLK}$. This count can be expressed as the reciprocal value of the product between the sensor's resolution N_{ds} and the frequency f_{re0} associated to a constant angular rotor speed ω_{re0} .

$$\tau_d = nT_{CLK} = \frac{1}{N_{ds}f_{re0}} \quad (2)$$

FPM can be implemented in different ways and three different methods have been considered in the following study.

(a). Taylor Series Expansion (TSE) Algorithm

In this approach, the estimated speed $\hat{\omega}_{re}(k)$ is computed according to the first order approximation of the Taylor series expansion, indicated in the following study as TSE1:

$$\hat{\omega}_{re}(k) \approx \frac{\Delta\theta_{re}(k)}{\Delta t(k)} \quad (3)$$

where k is the k th time elapsed between two consecutive position measurement updates.

(b). Least Square Fit (LSF) Algorithms

An alternative way to estimate the rotor speed is to construct a polynomial fitting of the input position/time data by using the least-squares fit (LSFs) method. In the LSFs technique an N^{th} -order polynomial can be fit through the M most recent data points $\theta_{re}(1), \theta_{re}(2), \dots, \theta_{re}(M)$ acquired from the rotor position sensor, where typically $M > N+1$ [20], [22]. Generally, with LSF N/M is defined a least-squares fit method with a N^{th} -order polynomial to fit M points of the acquisition rotor position data. For example, with LSF1/4 is defined as a least-squares fit method with a 1st-order polynomial ($N=1$) (a straight line) to fit four rotor position data points ($M=4$), or LSF1/8 is a 1st-order polynomial ($N=1$) (a straight line) to fit eight rotor position data points ($M=8$), etc. If with $t(k)$ is indicated the generic instant of time for which a generic pulse $\theta_{re}(k)=2\pi k/N_{ds}$ of the position sensor occurs, the estimated time

instant $\hat{t}(k)$ against which will occur next pulse is computed according to the polynomial fitting of $t(k)$, as:

$$\hat{t}(k) = a_0 + a_1 \theta_{re}(k) + a_2 \theta_{re}(k)^2 + \dots + a_N \theta_{re}(k)^N \quad (4)$$

where k is the generic rotor position data point, with $k=1, \dots, M$. Therefore, by considering M rotor position data points it is possible to define the linear system (5).

$$\begin{bmatrix} \hat{t}(1) \\ \hat{t}(2) \\ \vdots \\ \hat{t}(M) \end{bmatrix} = \begin{bmatrix} 1 & \theta_{re}(1) & \theta_{re}(1)^2 & \cdots & \theta_{re}(1)^N \\ 1 & \theta_{re}(2) & \theta_{re}(2)^2 & \cdots & \theta_{re}(2)^N \\ \vdots & \vdots & \vdots & \ddots & \vdots \\ 1 & \theta_{re}(M) & \theta_{re}(M)^2 & \cdots & \theta_{re}(M)^N \end{bmatrix} \begin{bmatrix} a_0 \\ a_1 \\ \vdots \\ a_N \end{bmatrix} \quad \hat{t} = \Theta \mathbf{a} \quad (5) \quad \Theta = \begin{bmatrix} 1 & 1 & 1^2 & \cdots & 1^N \\ 1 & 2 & 2^2 & \cdots & 2^N \\ \vdots & \vdots & \vdots & \ddots & \vdots \\ 1 & M & M^2 & \cdots & M^N \end{bmatrix} \quad (6)$$

where \hat{t} is the estimated time for each rotor position data points acquired, Θ is the coefficients matrix of the fitting polynomials, while \mathbf{a} is the vector of the unknown coefficients of the fitting polynomials. The consider matrix Θ depends on each rotor position data points and resolution N_{ds} . Generally, it is easier to rewrite the coefficients matrix Θ by normalizing it with respect to $2\pi/N_{ds}$, and Θ can be rewritten as shown in (6). The least squares method minimizes the sum of squared errors E , providing the coefficients of \mathbf{a} .

$$\mathbf{e} = \mathbf{t} - \hat{\mathbf{t}} \quad (7) \quad E = \sum \mathbf{e}^2 = \mathbf{e}^T \mathbf{e} = (\mathbf{t} - \Theta \mathbf{a})^T (\mathbf{t} - \Theta \mathbf{a}) \quad (8) \quad \mathbf{a} = (\Theta^T \Theta)^{-1} \Theta^T \mathbf{t} \quad (9)$$

The rotor speed estimation can be evaluated by considering the derivative of (4):

$$\frac{d \hat{t}(k)}{d \theta_{re}(k)} = 0 + a_1 + 2a_2 \theta_{re}(k) + \dots + Na_N \theta_{re}(k)^{N-1} \quad (10) \quad \frac{d \hat{t}}{d \Theta} = \mathbf{q}^T \bar{\Theta} \mathbf{t} \quad (11) \quad \mathbf{g} = (\mathbf{q}^T \bar{\Theta})^T \quad (12)$$

The previous polynomial coefficients \mathbf{a} can be substitute in (10) obtaining a generalized form (11), where $\mathbf{q}^T = [0 \ 1 \ 2M \ 3M^2 \ \dots \ NM^{N-1}]$ is the vector of coefficients of (10), while $\bar{\Theta} = (\Theta^T \Theta)^{-1} \Theta^T$. Finally, the coefficients to fit the rotor position data points are obtained in (12).

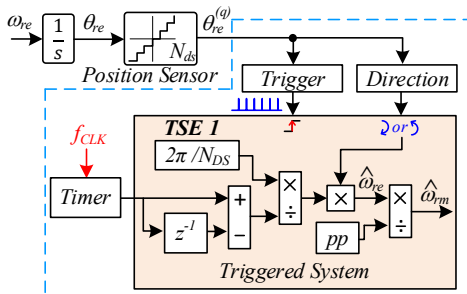


Fig. 1: FPM algorithm based on TSE1.

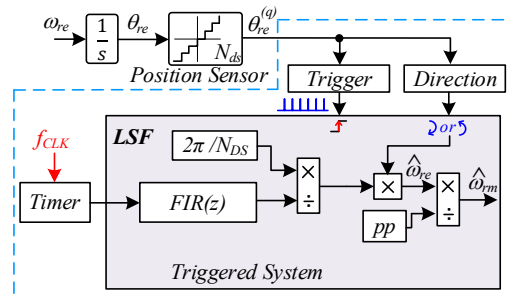


Fig. 2: FPM algorithm based on LSF.

It is shown in [2], [3] that the generic fitting polynomial $d \hat{t}(k)/d \Delta \theta_{re}(k)$ can be described through a finite impulsive response (FIR) digital filter. In this study two LSFs algorithms have been examined: LSF1/4 and LSF1/8. The first algorithm is based on a polynomial that fits four points on a straight-line, where the polynomial coefficients are $g_0 = 0.3$, $g_1 = 0.1$, $g_2 = -g_1$ and $g_3 = -g_0$ and the second algorithm LSF1/8 is implemented by considering a fitting polynomial of straight-line with eight points, where the polynomial coefficients are $g_0 = 0.0833$, $g_1 = 0.0595$, $g_2 = 0.0357$, $g_3 = 0.0119$, $g_4 = -g_3$, $g_5 = -g_2$, $g_6 = -g_1$ and $g_7 = -g_0$.

The discrete time function of the simplified FIR filter used in the LSF can be expressed as in (13), whose representation in the Laplace domain is given by (14).

$$FIR(z) = g_0 + g_1 z^{-1} + \dots + g_{M-1} z^{-(M-1)} \quad (13) \quad FIR(s) = g_0 + g_1 e^{-s \tau_d} + \dots + g_{M-1} e^{-(M-1)s \tau_d} \quad (14)$$

The speed estimation algorithms described above inherently introduce a delay equal or multiple of τ_d . Moreover, the accuracy of the estimated speed is related to the ratio between f_{CLK} and $1/\tau_d = N_{ds}f_{re0}$, which is strongly related to the motor speed, [18]-[29]. This becomes particularly evident at low rotational speed, as explained in the following sections.

Small-Signal Modeling

To represent the dynamic behaviour of FPM algorithms, their transfer functions around an operating point are determined by assuming that the shaft rotates at a constant speed $\omega_{re0}=2\pi f_{re0}$. The following approach can be extended in a straightforward way to several FPM implementations.

(a). TSE1

As described in [28] and [29], the small-signal transfer function of the TSE1 method can be determined by considering the effects of a) the counter, represented with a moving average filter $H_{aveg}(s)$, b) the triggered system represented with a sample and hold $H_{S&H}(s)$, and c) the control algorithm sampling time T_s , modelled with a further sample and hold $H_{Ts}(s)$. However, typical values of the sampling time T_s and clock time T_{CLK} are much smaller than τ_d , thus the effects of the control algorithm sampling time can be neglected, $H_{Ts}(s) \approx 0$, and the moving average filter can be approximated to a sample and hold, $H_{aveg}(s) \approx H_{S&H}(s)$, [28]-[29]. Therefore, the small-signal transfer function of TSE1, $H_{TSE1}(s)$, can be expressed as:

$$H_{TSE1}(s) = H_{aveg}(s) H_{S&H}(s) H_{Ts}(s) \approx H_{S&H}^2(s) = \frac{(1 - e^{-s\tau_d})^2}{s^2 \tau_d^2} \quad (14)$$

$H_{TSE1}(s)$ can be expressed in terms of its magnitude, $|H_{TSE1}(j\omega)|$, which is a sinc-squared function (15), and its phase $\angle H_{TSE1}(j\omega)$ (16).

$$|H_{TSE1}(j\omega)| = \frac{4}{\omega^2 \tau_d^2} \sin^2\left(\frac{\omega \tau_d}{2}\right) \quad (15) \qquad \angle H_{TSE1}(j\omega) = -\omega \tau_d \quad (16)$$

(b). LSF

The small-signal transfer function representing the LSF algorithm around an operating point can be determined by using same approach applied for TSE1. As shown in Fig. 2, the small-signal transfer function of the generic LSF algorithm depends on these three elements: a) the digital filter $FIR(z)$, b) the triggered system represented with a sample and hold $H_{S&H}(z)$, and c) the control algorithm sampling time T_s modelled by considering another sample and hold block $H_{Ts}(z)$. Even in this case the effect of $H_{Ts}(z)$ can be neglected compared to $H_{S&H}(z)$. According to the definition of the sample and hold discrete time transfer function $H_{S&H}(z) = 1 - z^{-1}$, [30], the discrete time small-signal transfer function of the LSF can be defined as:

$$H_{LSF}(z) = FIR(z) H_{S&H}(z) H_{Ts}(z) \approx FIR(z) H_{S&H}(z) = (g_0 + g_1 z^{-1} + \dots + g_{M-1} z^{-(M-1)}) (1 - z^{-1}) \quad (17)$$

Which can be rewritten as:

$$H_{LSF}(z) \approx H_{FIR}(z) H_{S&H}(z)^2 = [c_0 + c_1 z^{-1} + \dots + c_{M-2} z^{-(M-2)}] (1 - z^{-1})^2 \quad (18)$$

where $H_{FIR}(z)$ is a modified digital filter FIR function of $FIR(z)$ with coefficients defined as $c_0 = g_0$, $c_1 = (g_1 + g_0)$, ..., $c_{M-2} = (g_0 + g_1 + \dots + g_{M-2})$. Finally, the continuous time domain transfer function LSF around the operating point is obtained by considering the delay time τ_d as $z^{-1} = e^{-s\tau_d}$:

$$H_{LSF}(s) \approx H_{TSE1}(s) H_{FIR}(s) = \frac{(1 - e^{-s\tau_d})^2}{s^2 \tau_d^2} (c_0 + c_1 e^{-s\tau_d} + \dots + c_{M-2} e^{-(M-2)s\tau_d}) \quad (19)$$

From (19) it is possible to define the LSF1/4 small-signal transfer function:

$$H_{LSF1/4}(s) \approx H_{TSE1}(s) H_{FIR}(s) = \frac{(1 - e^{-s\tau_d})^2}{s^2 \tau_d^2} (0.3 + 0.4 e^{-s\tau_d} + 0.3 e^{-2s\tau_d}) \quad (20)$$

where the magnitude and phase for this speed estimator are:

$$|H_{LSF1/4}(j\omega)| = |H_{TSE1}(j\omega)| |0.4 + 0.6 \cos(\omega \tau_d)| \quad (21) \qquad \angle H_{LSF1/4}(j\omega) = -2\omega \tau_d \quad (22)$$

The magnitude obtained in (21) behaves like a sinc-square function but with an additional term that increases the filtering action of the LSF1/4 algorithm with respect to TSE1. As regards the phase, this transfer function highlights a delay twice compared to TSE1.

Similar procedure has been used to carried out the transfer function of the LSF1/8 algorithm, considering the delay action given by the different FIR filter structure. Its magnitude, $|H_{LSF1/8}(j\omega)|$ includes an additional term furtherly increasing the filtering action compared to TSE1 and LSF1/4. As regards the phase, a delay four time higher than TSE1 is observed.

$$|H_{LSF1/8}(j\omega)| = |H_{TSE1}(j\omega)| \cdot |0.1666\cos(3\omega\tau_d) + 0.2858\cos(2\omega\tau_d) + 0.3572\cos(\omega\tau_d) + 0.1905| \quad (23)$$

$$\angle H_{LSF1/8}(j\omega) = -4\omega\tau_d \quad (24)$$

Performance Analysis of FPM Algorithms

Starting from the small signal models, an in-depth analysis of FPMs performances can be carried out in terms of filtering action, closed loop stability analysis, torque load disturbance rejection. All these characteristics are strongly depending on the sensor finite resolution value N_{ds} .

(a). Filtering Action

The magnitude functions obtained in (15), (21) and (23) allow to evaluate the filtering action of each speed estimation algorithm on the quantization harmonics associated to the discontinuous position measurement. In particular, the study presented in [31] provided the analytical models of the quantized electrical rotor angle $\theta_{re}^{(q)}(t)$ and its time derivative, that is, the instantaneous quantized speed $\omega_{re}^{(q)}(t)$; these expressions are reported in (25) and (26) for a generic rotor position sensor of resolution N_{ds} , where it is assumed that the shaft rotates at ω_{re0} .

$$\theta_{re}^{(q)}(t) = \omega_{re0}t + \sum_{k=1}^{+\infty} \frac{2}{N_{ds}k} \sin(N_{ds}k\omega_{re0}t) \quad (25)$$

$$\omega_{re}^{(q)}(t) = \omega_{re0} + \sum_{k=1}^{+\infty} 2\omega_{re0} \cos(N_{ds}k\omega_{re0}t) \quad (26)$$

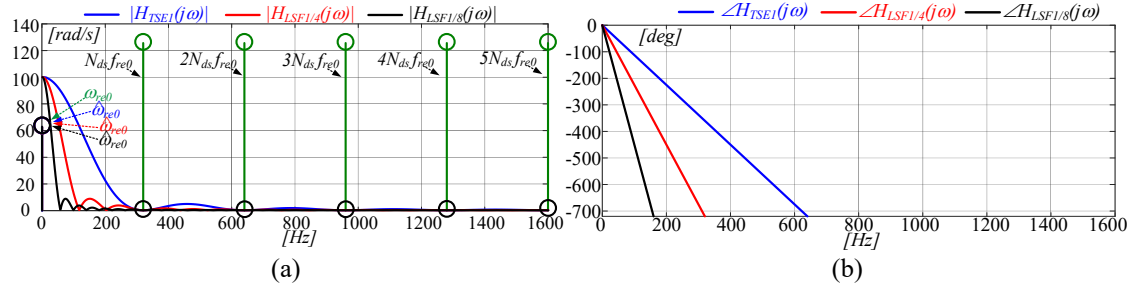


Fig. 3: Harmonic content of the instantaneous quantized $\omega_{re}^{(q)}$ and estimated speed $\hat{\omega}_{re}$ for the considered FPM algorithms: magnitudes $|H_{FPM}(j\omega)|$ (a); corresponding phases $\angle H_{FPM}(j\omega)$ (b).

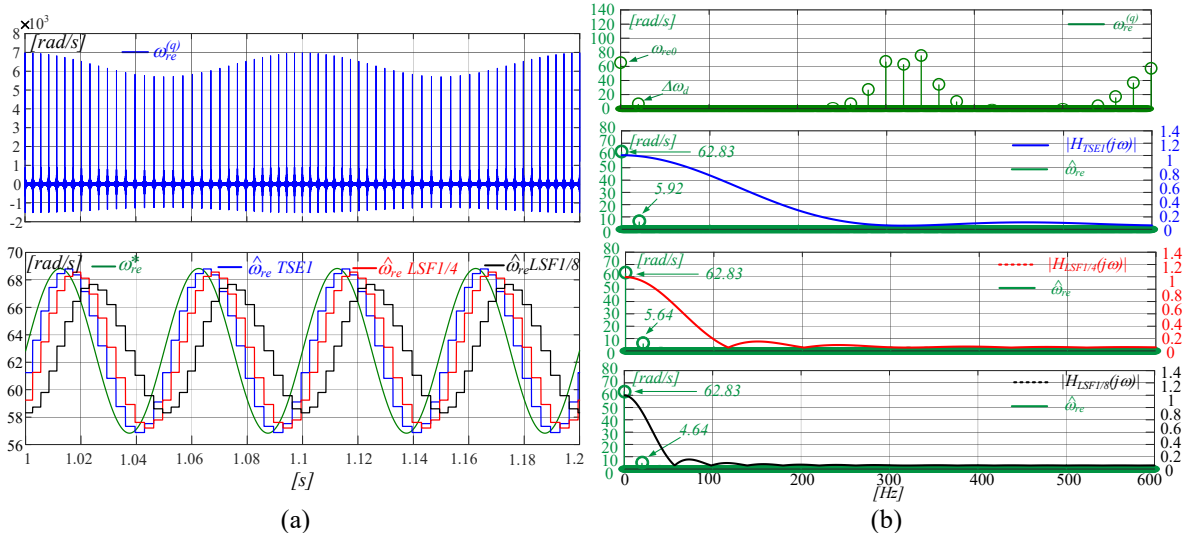


Fig. 4 Time waveforms (a) and harmonic spectrum (b) of the quantized $\omega_{re}^{(q)}$ and estimated speeds $\hat{\omega}_{re}$, considering $\omega_{re0} = 2\pi 10 \text{ rad/s}$ and a superimposed sinusoidal disturbance with magnitude $\Delta\omega_d = 0.1\omega_{re0}$ and frequency $\omega_d = 2\pi 10 \text{ rad/s}$.

The magnitude spectrum of $\omega_{re}^{(q)}(t)$ is displayed in Fig. 3a for $\omega_{re0}=2\pi 10 \text{ rad/s}$, and $N_{ds}=32$. The instantaneous quantized speed $\omega_{re}^{(q)}(t)$ features an infinite number of equally spaced quantization harmonics at $kN_{ds}\omega_{re0}$, each having an amplitude equal to $2\omega_{re0}$; the only physically meaningful harmonic is the dc component ω_{re0} . When the FPM methods are applied to $\omega_{re}^{(q)}$, the sinc-squared functions (15), (21) and (23) filter $\omega_{re}^{(q)}(t)$ by cancelling all quantization harmonics. It is worth noting that LSF1/4 and LSF1/8 feature a greater filtering action in the low frequency range.

With regards to the phase $\angle H_{FPM}(j\omega)$, delays equal to τ_d , $2\tau_d$ or $4\tau_d$ are included in the speed estimation loop with TSE1, LSF1/4, and LSF1/8 respectively. These delays have a significant impact on the stability of the speed closed loop, as will be outlined below.

Filtering action of FPMs can have a detrimental impact even on the estimation of external torque disturbances applied to the rotor shaft. Fig. 4 deals with this issue, displaying the waveforms and harmonic spectrums of the quantized $\omega_{re}^{(q)}$ and estimated speeds $\hat{\omega}_{re}$ carried out with the considered FPMs, when a speed sinusoidal disturbance is superimposed to ω_{re0} . An effective suppression of the quantization harmonics in the estimated speed are observed even in this operating condition for all FPM algorithms, Fig. 4b, even though TSE1 provides a more accurate estimation of the speed disturbance, Fig. 4a.

(b). Speed Controller Design

The stability analysis of the closed speed loop including the FPM algorithms has been performed by exploiting the modelling described in the previous section. In particular, the design of speed loop controller $C(s)$ is accomplished according to the speed loop bandwidth f_{BW} requested by the drive specifications. It is assumed that the actual shaft rotor speed is the feedback, and the mechanical system $P(s)$ is represented only with its inertia J , neglecting mechanical frictions, (27). The inner current control loop is also neglected as its bandwidth is significantly higher than external speed loop. A small signal closed loop control structure including the FPM algorithm is displayed in Fig. 5.

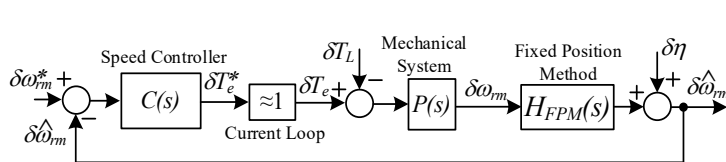


Table I Control Loop Setting

$f_{BW} [\text{Hz}]$	15	20	30
k_p	0.218	0.291	0.437
k_i	1.57	2.79	6.29

Fig. 5: Small signal closed loop control including FPM algorithms.

The proportional k_p and integral k_i gains of the PI controller $C(s)$ can be computed by imposing the two poles of the closed loop transfer function $W(s)$ (28):

$$P(s) = \frac{I}{sJ} \quad (27) \quad C(s) = \frac{k_ps+k_i}{s} \quad F(s) = C(s)P(s) = \frac{k_ps+k_i}{s^2J} \quad W(s) = \frac{F(s)}{1+F(s)} = \frac{k_ps+k_i}{s^2J+k_ps+k_i} \quad (28)$$

In particular, $F(s)$ and $W(s)$ are represented in terms of the poles p_1 and p_2 as indicated in (29), allowing to express the crossover angular frequency $\omega_{ci} = 2\pi f_{ci}$ and the closed loop bandwidth $\omega_{BW} = 2\pi f_{BW}$ as indicated in (31) and (33) respectively, [30], [32].

$$F(s) = \frac{(p_1+p_2)s+p_1p_2}{s^2} \quad W(s) = \frac{(p_1+p_2)s+p_1p_2}{s^2+(p_1+p_2)s+p_1p_2} \quad k_p = (p_1 + p_2) J \quad k_i = p_1 p_2 J \quad (29)$$

$$|F(j\omega_{ci})| = 1 \quad (30) \quad f_{ci} = \frac{1}{2\pi} \sqrt{\frac{(p_1+p_2)^2 + \sqrt{(p_1+p_2)^4 + 4(p_1p_2)^2}}{2}} \quad (31)$$

$$|W(j\omega_{BW})| = \frac{\sqrt{2}}{2} \quad (32) \quad f_{BW} = \frac{1}{2\pi} \sqrt{\frac{p_1^2 + p_2^2 + 4p_1p_2 + \sqrt{(p_1^2 + p_2^2 + 4p_1p_2)^2 + 4(p_1p_2)^2}}{2}} \quad (33)$$

A common approach in the selection of these two closed loop poles is to space them one decade apart from each other on the negative real axis, i.e. $p_2 = 0.1p_1$; in this way, it is possible from (33) to obtain an easy relationship linking the fastest pole p_1 and the closed loop bandwidth: $p_1 \approx 1.68\pi f_{BW}$. From the last expression, it is possible to set the speed controller gains k_p and k_i according to (29). Table I lists the gain values computed for different bandwidths f_{BW} .

(c). Stability Analysis

A metric providing the closed loop stability margin is given by the phase margin $m_{\varphi i}$ associated to the open loop transfer function $F(s)$:

$$m_{\varphi i} = \angle F(j\omega_{ci}) + \pi = \text{atan}\left(\frac{\omega_{ci}k_p}{k_i}\right) \quad (34)$$

In order to evaluate the FPMs speed estimator influence on the closed loop stability, it is necessary to include the transfer functions $H_{FPM}(s)$ of speed estimators in the above analysis, as displayed in Fig. 5. The corresponding open loop $F_{FPM}(s)$ and closed loop $W_{FPM}(s)$ transfer functions are respectively given by:

$$F_{FPM}(s) = C(s) P(s) H_{FPM}(s) \quad (35)$$

$$W_{FPM}(s) = \frac{C(s) P(s) H_{FPM}(s)}{1 + C(s) P(s) H_{FPM}(s)} \quad (36)$$

The phase margin m_{φ} and crossover angular frequency ω_c are modified compared to the ideal speed closed loop, because of the delay time τ_d which impacts on the magnitude and phase of the open loop frequency responses. As an example, Fig. 6 displays magnitude and phase of $F(s)$ and $F_{FPM}(s)$ for two speed loop bandwidths f_{BW} , in case of $m_{\varphi}=0^\circ$ and $m_{\varphi}=60^\circ$; these values of m_{φ} correspond to very different values of τ_d . The figures display the crossover frequencies f_c when $H_{FPM}(s)$ are included in the open loop transfer function. The comparison between $F(s)$ and $F_{FPM}(s)$ highlights limited differences between the ideal crossover frequencies f_{ci} and f_c , especially at high phase margins m_{φ} .

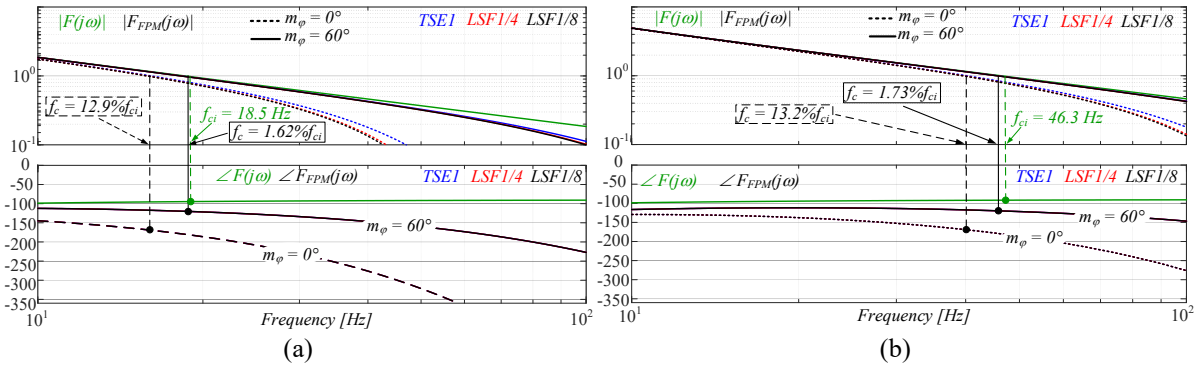


Fig. 6: Magnitude and phase comparisons between $F(s)$ and different $F_{FPM}(s)$ algorithms (TSE1, LSF1/4 and LSF1/8), (a) at $f_{BW}=20\text{Hz}$, for different m_{φ} and (b) at $f_{BW}=50\text{Hz}$ for different m_{φ} .

As a consequence, we can approximate $f_c \approx f_{ci}$ and thus compute the phase of $F_{FPM}(s)$ at f_{ci} and its corresponding phase margin:

$$\angle F_{FPM}(j\omega_{ci}) = \text{atan}\left(\frac{\omega_{ci}k_p}{k_i}\right) - \angle H_{FPM}(j\omega_{ci}) - \pi \quad m_{\varphi} = \angle F_{FPM}(j\omega_{ci}) + \pi = m_{\varphi i} - \angle H_{FPM}(j\omega_{ci}) \quad (37)$$

Considering the phase delay defined for each FPM algorithms analysed in this paper, the corresponding phase margin evaluated at the ideal cross-over frequency f_{ci} , are:

$$\text{TSE1: } m_{\varphi} = m_{\varphi i} - \omega_{ci} \tau_d \quad \text{LSF1/4: } m_{\varphi} = m_{\varphi i} - 2\omega_{ci} \tau_d \quad \text{LSF1/8: } m_{\varphi} = m_{\varphi i} - 4\omega_{ci} \tau_d \quad (38)$$

The relationships (38) highlight the detrimental impact of τ_d on the stability margin and thus on the closed-loop damping ratio and rise time. For a given value of m_{φ} requested by the motor drive specifications at the lowest rotating speed ω_{rm0} , which is usually around $60^\circ \div 80^\circ$, the max value of allowed delay time τ_{dmax} can be determined for each considered FPM as:

$$\tau_{dmaxTSE1} = \frac{\text{atan}\left(\frac{2\pi f_{ci} k_p}{k_i}\right) - m_{\varphi}}{2\pi f_{ci}}; \quad \tau_{dmaxLSF1/4} = \frac{\tau_{dmaxTSE1}}{2}; \quad \tau_{dmaxLSF1/8} = \frac{\tau_{dmaxTSE1}}{4} \quad (39) \quad \omega_{rm0} = \frac{2\pi}{pp \tau_{dmax} N_{ds}} \quad (40)$$

By exploiting (2), it is possible to link ω_{rm0} to sensor resolution N_{ds} , according to (40). Hence, for a specific set of N_{ds} and f_{BW} , the lowest operating speed ω_{rm0} will be different depending on the speed estimation algorithm.

(d). Torque Load Disturbance Rejection

Finally, the capability of the drive to mitigate the effects of load disturbances can be analysed by means of the dynamic stiffness transfer function. According to the control structure of Fig. 5, the dynamic stiffness is defined as:

$$DS_{FPM}(s) = \frac{\delta T_L(s)}{\delta \omega_{rm}(s)} = \frac{1 + F_{FPM}(s)}{P(s)} = \frac{1 + C(s) P(s) H_{FPM}(s)}{P(s)} \quad (41)$$

which is also affected by τ_d , as will be clearly underlined in the experimental tests.

Experimental Results

The above presented theoretical study has been validated through a wide campaign of experimental tests. In particular, a test bench has been arranged consisting of two PMSM drives whose shafts are mechanically coupled and sharing same DC bus. Motors specifications are summarized in Tables II and III. Both motor drives are fed by SiC inverters operated at 20kHz. A dSpace DS1006 have been used to control the IPM drive under test and implementing the FPMs algorithms with a f_{CLK} equal to 1MHz. Both electric drives are equipped with incremental encoders featuring $N_{ds} = 2048$, and different position sensor resolutions have been obtained by downsampling the encoder position measurement. Rotor field oriented control has been implemented in the drive under test, as displayed in Fig. 9, where the execution time of the current and speed loops are respectively $100\mu s$ and $200\mu s$. In all tests the current control loop bandwidth is fixed at 500Hz.

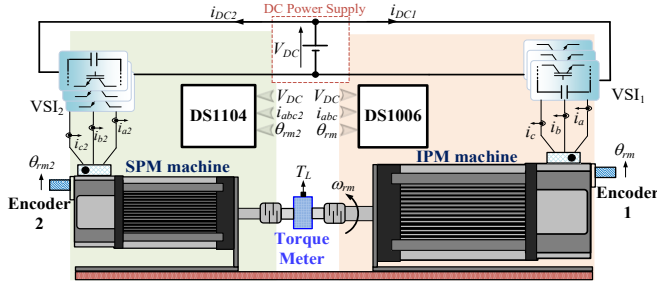


Fig. 7: Variable speed drive test bench.

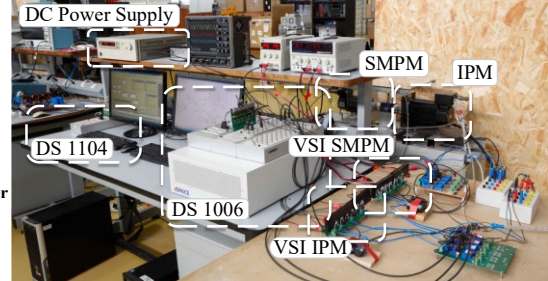


Fig. 8: Test bench setup.

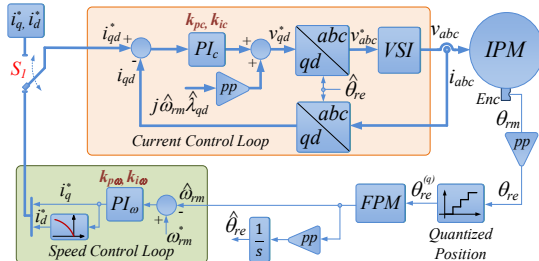


Fig. 9: Block diagram control of the drive under test.

Table II: SPM Motor Drive Data

P_n	2 kW
ω_n	6000 rpm
T_n	5 Nm
R_s	0.84Ω
L_s	4.7 mH
pp	3
J	3.4 kgcm^2

Table III: IPM Motor Drive Data

P_n	3.6 kW
ω_n	2000 rpm
T_n	19.1 Nm
R_s	2.4Ω
L_s	12.189 mH
pp	3
J	21.7 kgcm^2

(a). Stability Limits of FPM Algorithms

Tests were undertaken to verify the effectiveness of the closed loop stability study. In particular, Fig. 10 depicts the stability limits ($m_\phi = 0^\circ$) of the speed control loop implemented in the experimental setup (circle marks) for different rotor position sensor resolutions N_{ds} and by using different speed estimation algorithms; the same figure displays the stability limits determined by using the proposed analytical approach. The speed loop bandwidth is set at $f_{BW} = 20\text{Hz}$ for each N_{ds} configuration. It is noted that a good agreement between modelling and experimental tests is achieved for medium-low values of N_{ds} , while at higher N_{ds} the limited resolution of the encoder combined to the downsampling of the rotor position measurement and $f_{CLK}=1\text{MHz}$ yield to higher errors between simulations and experimental results. It has been verified via simulation that by increasing the f_{CLK} to 100MHz a significant reduction of the differences between simulations and experimental tests is achieved even for

high N_{ds} (filled rhombus). It is worth noting that LSF-based methods underline greater instability region at low rotational speed compared to TSE1. Same figures display the minimum rotational speeds predicted by (40) guaranteeing specific value of m_φ .

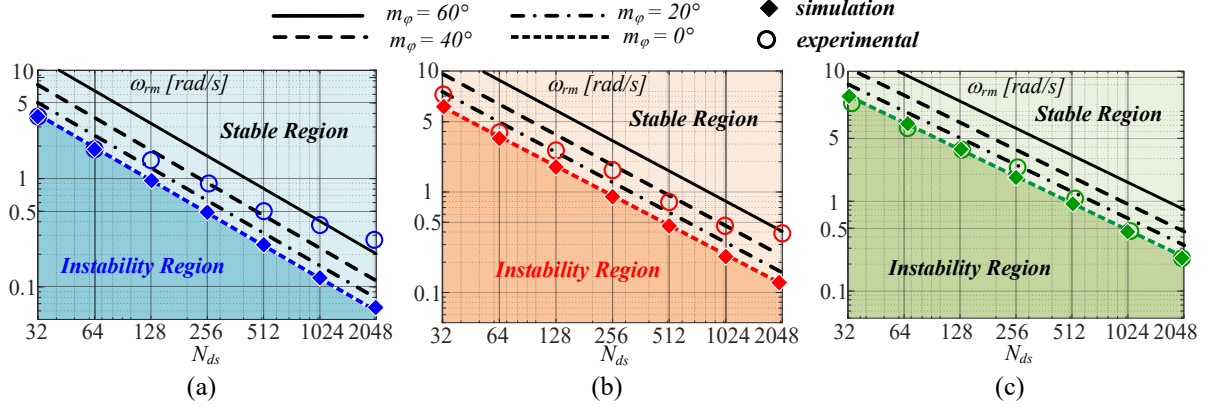


Fig. 10: Rotor speed stability vs instability regions at $f_{BW}=20\text{Hz}$: (a) TSE1, (b) LSF1/4 and (c) LSF1/8.

Further tests have been performed to validate the design of speed control loop including the FPM algorithms. In the following tests the drive is set according to the proposed approach to feature a closed speed loop bandwidth $f_{BW} = 20\text{Hz}$ ($k_p=0.29$, $k_i=2.79$), $N_{ds}=32$, and a phase margin $m_\varphi = 60^\circ$ for the three considered speed loops. Based on the type of FPM, the fulfilment of these drive specifications is obtained by considering different reference speed ω_{rm}^* according to (40): 17rad/s, 34rad/s and 69rad/s for TSE1, LSF1/4 and LSF1/8 respectively. With these settings we expect to observe the same dynamic behaviour in all speed loops, even though they include different FPM algorithms. For each speed loop operating at ω_{rm}^* , an additional sinusoidal speed disturbance of magnitude $\Delta\omega_{rm} = 5\text{rad/s}$ and frequency variable from 1Hz to 100 Hz is superimposed to the reference speed to experimentally determine $|W_{FPM}(j\omega)|$.

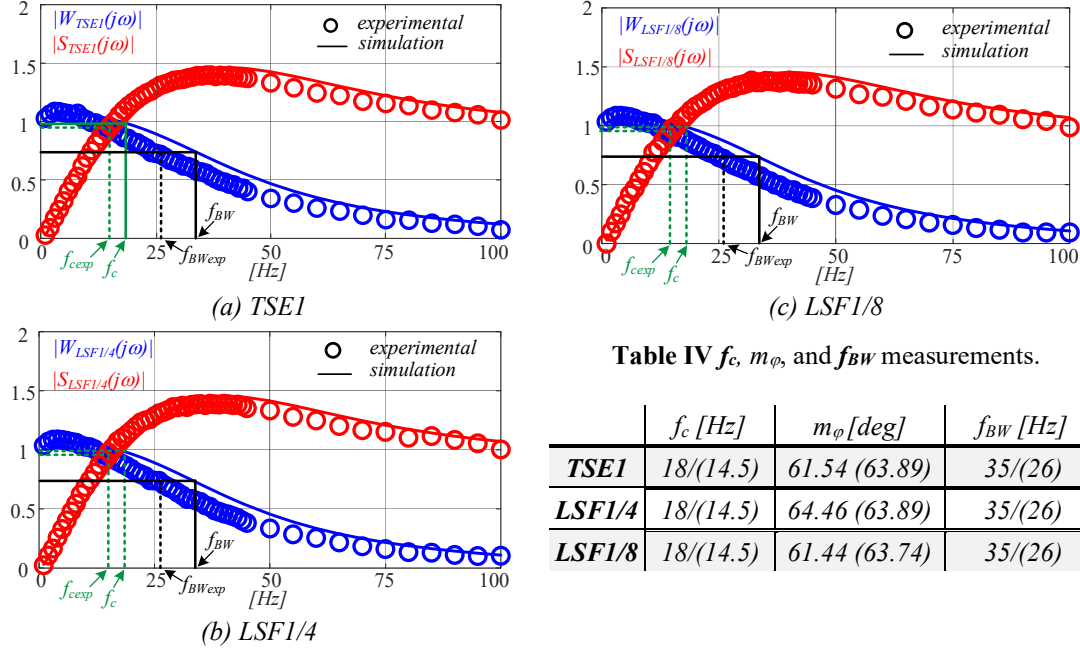


Table IV f_c , m_φ , and f_{BW} measurements.

	$f_c [\text{Hz}]$	$m_\varphi [\text{deg}]$	$f_{BW} [\text{Hz}]$
TSE1	18/(14.5)	61.54 (63.89)	35/(26)
LSF1/4	18/(14.5)	64.46 (63.89)	35/(26)
LSF1/8	18/(14.5)	61.44 (63.74)	35/(26)

Fig. 11 Comparison between the magnitude of the sensitivity $|S_{FPM}(s)|$ and closed loop $|W_{FPM}(s)|$ transfer functions carried out through the small signal models (within brackets) and experimental tests, with the following reference design specifications: $f_{BW}=20\text{Hz}$, $m_\varphi=60^\circ$ and $N_{ds}=32$.

Then, a further campaign of measurement has been conducted for each speed loop by setting a constant ω_{rm}^* , and adding the same sinusoidal disturbance in the feedback speed $\hat{\omega}_{rm}$. In this way, the sensitivity transfer function $S_{FPM}(s)$ has been experimentally carried out $S_{FPM}(j\omega) = 1/(1 + F_{FPM}(j\omega))$. It is demonstrated by the control systems theory [32] that the cross point between the frequency responses

$|W_{FPM}(j\omega)|$ and $|S_{FPM}(j\omega)|$ provides the cross-over frequency f_c and the vector stability margin VM ($VM = 1/|W(j\omega_0)|$); the last quantity, in turns, can be related to m_ϕ by the following relationship: $m_\phi = \arcsin(VM/2)$. Fig. 11 displays $|W_{FPM}(j\omega)|$ and $|S_{FPM}(j\omega)|$ for each FPM considered in this study. The cross-over frequency $f_{cexp} = 14.5\text{Hz}$ carried out with experimental tests is pretty much the same for all FPMs, confirming the theoretical analysis, whose deviation from the theoretical value $f_c = 18\text{Hz}$ is lower than 20%. Looking at the phase margin determined from experimental test $m_{\phi,exp} = 63.8^\circ$, the last is slightly higher compared the one used in (38)-(40). These tests confirm that TSE1 allows to achieve same dynamic performances compared to FPMs based on LSF, at lower operational speed. The f_{BW} can be experimentally evaluated by considering the frequency of $|W_{FPM}(j\omega)|$ when the condition $|W(j\omega_{BW})| = (\sqrt{2}/2)$ occurs. The tests underlined an increase of the speed loop bandwidth of the experimental test-bench f_{BWexp} higher than 30% compared to the requested f_{BW} , which can be considered fully satisfying the motor drive specifications.

(b). Torque Load Disturbance Rejection

Dynamic stiffness curves have been carried out by applying a sinusoidal torque disturbance featuring a magnitude of $\Delta T_L = 3\text{Nm}$ and a variable frequency range from 1Hz to 200 Hz with the drive controlled at a low and constant rotational speed $\omega_{rm}^* = 20\text{rad/s}$ and $N_{ds} = 32$. Fig. 12 summarizes the results of this analysis, where the theoretical curve (41) has been compared to the experimental tests. You can note that all methods feature a good disturbance rejection capability at medium high frequencies, while note a worsen behaviour in LSF-based algorithms around the medium frequencies because they feature a reduced phase margin m_ϕ .

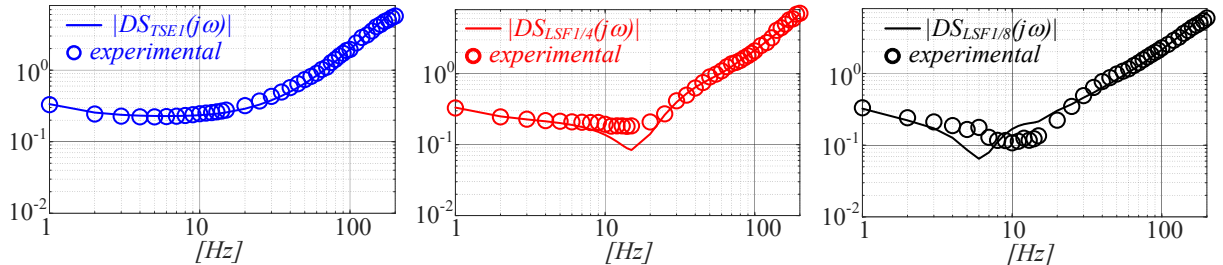


Fig. 12 Experimental vs theoretical Dynamic Stiffness magnitude for different FPM algorithms.

Conclusion

This paper has investigated the performances of speed-controlled motor drives using non-model-based speed estimation algorithms. Key observations include the following.

- Small signal modelling around an operating point of the speed closed loop allows to predict its filtering action, closed loop stability analysis, and torque load disturbance rejection, as a function of the requested motor drive specifications at the lowest rotating speed ω_{rmo} and position sensor resolution N_{ds} .
- The algorithm TSE1 features lower filtering action of the quantization speed harmonics compared to the LSF-based methods which limits its capability to mitigate the effects of measurement nonidealities and noise. On the other hand, its greater stability region allows the drive to operate at lower operating speeds.

Experimental results have confirmed the key results of this theoretical investigation.

References

- [1] R.D. Lorenz and K. Van Patten, "High-resolution velocity estimation for all-digital, ac servo drives," IEEE Trans. Ind. Appl., vol. 27, no. 4, pp. 701 – 705, Jul./Aug. 1991.
- [2] M. Cacciato, A. Consoli, G. Scarella and G. Scelba, "Indirect Maximum Torque per Ampere control of induction motor drives," 2007 European Conference on Power Electronics and Applications, 2007, pp. 1-10.
- [3] P. L. Jansen and R. D. Lorenz, "Transducerless position and velocity estimation in induction and salient AC machines," in IEEE Transactions on Industry Applications, vol. 31, no. 2, pp. 240-247, March-April 1995.

- [4] Hyunbae Kim, Sungmo Yi, Namsu Kim and R. D. Lorenz, "Using low resolution position sensors in bumpless position/speed estimation methods for low cost PMSM drives," Fourtieth IAS Annual Meeting. Conference Record of the 2005 Industry Applications Conference, 2005., 2005, pp. 2518-2525 Vol. 4.
- [5] B. Akin et al., "Low Speed Performance Operation of Induction Motors Drives Using Low-Resolution Speed Sensor," 2006 IEEE International Symposium on Industrial Electronics, 2006, pp. 2110-2115.
- [6] M. Pulvirenti et al., "On-line stator resistance and permanent magnet flux linkage identification on open-end winding PMSM drives," IEEE Energy Conversion Congress and Exposition (ECCE), 2017, pp. 5869-5876.
- [7] S. Morimoto et al., "Sensorless control strategy for salient-pole PMSM based on extended EMF in rotating reference frame," in IEEE Trans. on Industry Applications, vol. 38, no. 4, pp. 1054-1061, July-Aug. 2002.
- [8] Jianrong Bu, Longya Xu, T. Sebastian and Buyun Liu, "Near-zero speed performance enhancement of PM synchronous machines assisted by low-cost Hall effect sensors," APEC '98 Thirteenth Annual Applied Power Electronics Conference and Exposition, 1998, pp. 64-68 vol.1.
- [9] G. Scarella, G. Scelba and A. Testa, "High performance sensorless controls based on HF excitation: A viable solution for future AC motor drives?," 2015 IEEE Workshop on Electrical Machines Design, Control and Diagnosis (WEMDCCD), 2015, pp. 178-187.
- [10] Y. -C. Kwon, J. Lee and S. -K. Sul, "Recent Advances in Sensorless Drive of Interior Permanent-Magnet Motor Based on Pulsating Signal Injection," in IEEE Journal of Emerging and Selected Topics in Power Electronics, vol. 9, no. 6, pp. 6577-6588, Dec. 2021.
- [11] D. Raca et al., "Carrier-Signal Selection for Sensorless Control of PM Synchronous Machines at Zero and Very Low Speeds," in IEEE Trans. on Industry Applications, vol. 46, no. 1, pp. 167-178, Jan.-feb. 2010.
- [12] J. Holtz, "Sensorless Control of Induction Machines—With or Without Signal Injection?," in IEEE Transactions on Industrial Electronics, vol. 53, no. 1, pp. 7-30, Feb. 2006.
- [13] J. Holtz, "Developments in Sensorless AC Drive Technology," 2005 International Conference on Power Electronics and Drives Systems, 2005, pp. 9-16.
- [14] L. D. Tornello et al., "Combined Rotor-Position Estimation and Temperature Monitoring in Sensorless, Synchronous Reluctance Motor Drives," in IEEE Trans. on Ind. Appl., vol. 55, pp. 3851-3862, 2019.
- [15] Avago Technologies Motion Control Encoders in Electrical Motor Systems: Design Guide.
- [16] G. Scelba, G. De Donato, G. Scarella, F. Giulii Capponi and F. Bonaccorso, "Fault-Tolerant Rotor Position and Velocity Estimation Using Binary Hall-Effect Sensors for Low-Cost Vector Control Drives," in IEEE Transactions on Industry Applications, vol. 50, no. 5, pp. 3403-3413, Sept.-Oct. 2014.
- [17] G. De Donato et al., "Low-Cost, High-Resolution, Fault-Robust Position and Speed Estimation for PMSM Drives Operating in Safety-Critical Systems," in IEEE Trans. on Pow. Electr., vol. 34, pp. 550-564, 2019.
- [18] R. Petrella, M. Tursini, L. Peretti and M. Zigliotto, "Speed measurement algorithms for low-resolution incremental encoder equipped drives: a comparative analysis," 2007 International Aegean Conference on Electrical Machines and Power Electronics, 2007, pp. 780-787.
- [19] L. Bascetta et al., "Velocity Estimation: Assessing the Performance of Non-Model-Based Techniques," in IEEE Transactions on Control Systems Technology, vol. 17, no. 2, pp. 424-433, March 2009.
- [20] R. H. Brown, S. C. Schneider and M. G. Mulligan, "Analysis of algorithms for velocity estimation from discrete position versus time data," in IEEE Trans. on Ind. Electronics, vol. 39, no. 1, pp. 11-19, Feb. 1992.
- [21] S. M. Phillips and M. S. Branicky, "Velocity estimation using quantized measurements," 42nd IEEE International Conference on Decision and Control (IEEE Cat. No.03CH37475), 2003, pp. 4847-4852 Vol.5.
- [22] P. S. Carpenter et al., "On algorithms for velocity estimation using discrete position encoders," Proceedings of IECON '95 - 21st Annual Conference on IEEE Industrial Electronics, 1995, pp. 844-849 vol.2.
- [23] Q. Ni et al., "A New Position and Speed Estimation Scheme for Position Control of PMSM Drives Using Low-Resolution Position Sensors," in IEEE Trans. on Ind. Appl., vol. 55, pp. 3747-3758, July-Aug. 2019.
- [24] A. Anuchin, A. Dianov and F. Briz, "Synchronous Constant Elapsed Time Speed Estimation Using Incremental Encoders," in IEEE/ASME Trans. on Mechatronics, vol. 24, no. 4, pp. 1893-1901, Aug. 2019.
- [25] A. Anuchin, V. Astakhova, D. Shpak, A. Zharkov and F. Briz, "Optimized method for speed estimation using incremental encoder," 2017 International Symposium on Power Electronics (Ee), 2017, pp. 1-5.
- [26] Y. Vázquez-Gutiérrez et al., "Small-Signal Modeling of the Incremental Optical Encoder for Motor Control," in IEEE Trans. on Industrial Electronics, vol. 67, no. 5, pp. 3452-3461, May 2020.
- [27] L. D. Tornello, G. Scelba, G. D. Donato, F. G. Capponi, G. Scarella and M. Harbaugh, "Selection of Rotor Position Sensor Resolution for Variable Frequency Drives Utilizing Fixed-Position-Based Speed Estimation," 2021 IEEE Energy Conversion Congress and Exposition (ECCE), 2021, pp. 4846-4853.
- [28] Gene F. Franklin, J. D. Powell, Michael Workman, "Digital Control of Dynamic Systems", Third Ed., 1998.
- [29] G. Scelba et al., "Resolution of Rotor Position Measurement: Modeling and Impact on Speed Estimation," in IEEE JESTPE, vol. 10, no. 2, pp. 1992-2004, April 2022.
- [30] Karl Johan Astrom, Richard M. Murray, "Feedback Systems: An Introduction for Scientists and Engineers", February, 2009.